



Ultrahigh-rate and high-frequency MXene micro-supercapacitors for kHz AC line-filtering

Xin Feng^{a,b,d,e}, Sen Wang^b, Pratteek Das^b, Xiaoyu Shi^b, Shuanghao Zheng^{b,c}, Feng Zhou^b, Jing Ning^{d,e,*}, Dong Wang^{d,e,f}, Jincheng Zhang^{a,d,e}, Yue Hao^{a,d,e}, Zhong-Shuai Wu^{b,c,*}

^aGuangzhou Wide Bandgap Semiconductor Innovation Center, Xidian University, Xi'an 710071, Shaanxi, China

^bState Key Laboratory of Catalysis, Dalian Institute of Chemical Physics, Chinese Academy of Sciences, Dalian 116023, Liaoning, China

^cDalian National Laboratory for Clean Energy, Chinese Academy of Sciences, Dalian 116023, Liaoning, China

^dState Key Discipline Laboratory of Wide Band Gap Semiconductor Technology, Xidian University, Xi'an 710071, Shaanxi, China

^eShaanxi Joint Key Laboratory of Graphene, Xidian University, Xi'an 710071, Shaanxi, China

^fXidian-Wuhu Research Institute, Wuhu 241000, Anhui, China

ARTICLE INFO

Article history:

Received 22 September 2021

Revised 2 November 2021

Accepted 8 November 2021

Available online 16 November 2021

Keywords:

MXene

Micro-supercapacitors

Ionic liquid

Photolithography

AC line-filtering

Energy storage

ABSTRACT

Harnessing energy from the environment promotes the rapid development of micro-power generators and relevant power management modules of alternating current (AC) line-filtering to obtain a stabilized direct current (DC) output for storage and use. Micro-supercapacitors (MSCs) with miniaturized volume and high-frequency response are regarded as a critical component in filtering circuits for microscale power conversion. Here, we reported the fabrication of the wafer-sized planar MSCs (M-MSCs) based on 2D Ti₃C₂T_x MXene using a photolithography technique. The M-MSCs exhibited an areal capacitance of 153 μF cm⁻² and a frequency characteristic (f_0) of 5.6 kHz in aqueous electrolyte. Moreover, by employing suitable ionic liquid as electrolyte, the voltage window was expanded to 2 V and the f_0 could be pushed to 6.6 kHz relying on the electrical double-layer mechanism and lower adsorption energy while maintaining quasi-rectangular cyclic voltammogram curves at 5000 V s⁻¹. Furthermore, the integrated MSCs pack was constructed and exhibited excellent rectifying ability by filtering various high-frequency 5000 Hz AC signals with different waveforms into stable DC outputs. Such ultrahigh-rate and high-voltage M-MSCs module for kHz AC line-filtering would be potentially integrated with customizable electronics to realize on-chip rectifiers in high-density integrated circuit.

© 2021 Science Press and Dalian Institute of Chemical Physics, Chinese Academy of Sciences. Published by ELSEVIER B.V. and Science Press. All rights reserved.

1. Introduction

The demand for self-powered, miniaturized, and integrable electronic systems has been increasing steadily fueled by the rapid development of emerging technologies like internet of things [1–4]. Usually, these electronic systems consist of sensors, microelectronics, micro-scale power generation, management and storage devices [5–9]. The power generating devices such as triboelectric nanogenerators can convert mechanical energy in the environment into electric power/signal which manifests as a pulsed high-voltage alternating current (AC) output in the frequency range of tens to hundreds of hertz. This needs to be rectified to direct current (DC) through an AC line-filtering circuit before being stored and subsequently utilized [10–12]. The critical component in the

filtering circuit is a filter capacitor (FC) to enable electric conversion and noise filtering. However, the conventional FCs, such as aluminum electrolytic capacitors (AECs) not only are rigid and large, but also offer low capacitance and slow frequency response, hindering their application in miniaturized and portable electronic systems. Moreover, the poor frequency characteristic of AECs (usually characteristic frequency (f_0) < 1 kHz) makes it powerless in satisfying variable frequency demands. It is therefore important to replace these bulky capacitive devices by fabricating miniaturized FCs using advanced microelectronic manufacture technology.

Micro-supercapacitors (MSCs) have been widely researched as the micro energy storage devices thanks to the fast charge/discharge rates, high-power density and cycling stability [13–19]. By virtue of the representative feature of rapid frequency response, MSCs functioning as FCs are gradually receiving more attention, which is resulting from the short distance between microelectrodes [20–22]. In addition, MSCs are more suitable for integration

* Corresponding authors.

E-mail addresses: ningj@xidian.edu.cn (J. Ning), wuzs@dicp.ac.cn (Z.-S. Wu).

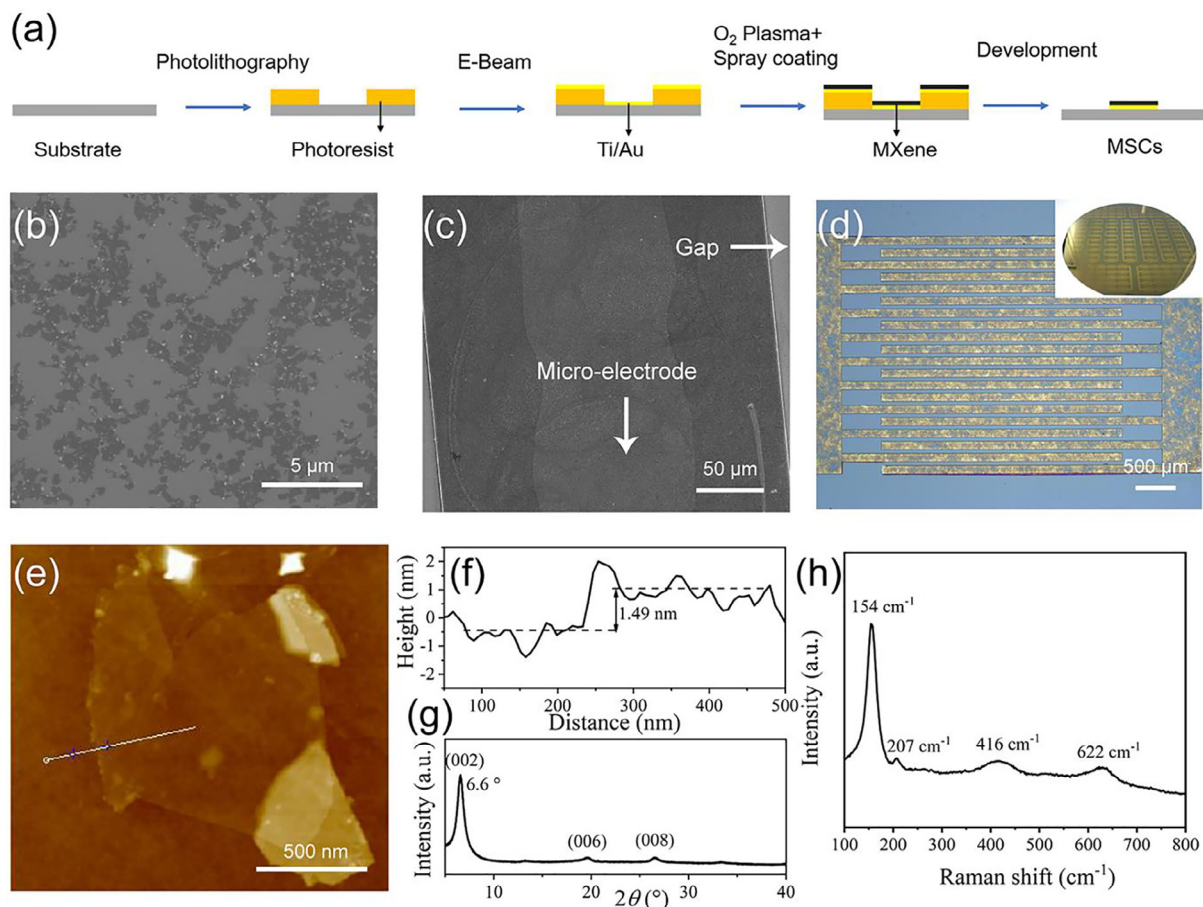


Fig 1. (a) Schematic illustration of fabrication process of the on-chip M-MSCs by photolithography technology. (b) SEM image of $\text{Ti}_3\text{C}_2\text{T}_x$ MXene nanosheets. (c) SEM image of the $\text{Ti}_3\text{C}_2\text{T}_x$ MXene microelectrodes. (d) The optical image of M-MM-MSCs (width: 100 μm , gap: 50 μm). Inset photograph shows M-MSCs array on the 4-inch silicon wafer substrate. (e) AFM image and (f) height profile of $\text{Ti}_3\text{C}_2\text{T}_x$ MXene nanosheets. (g) XRD pattern and (h) Raman spectrum of $\text{Ti}_3\text{C}_2\text{T}_x$ microelectrodes.

with miniaturized and portable electronic systems based on various compatible manufacturing techniques including photolithography [23,24], inkjet printing [25,26], and direct laser writing [27–29]. According to the significant requirements in front-end power generators for the conversion of wide frequency and high-voltage input signals, MSCs with wide operating voltage and wide workable frequency are crucial to adequately satisfy AC line-filtering circuits.

For realizing the high frequency feature, highly conductive materials with large specific surface area are utilized as microelectrodes in MSCs owing to the fast charge transfer ability and sufficient active sites for ions adsorption [30–34]. As a typical member of two-dimensional (2D) transition metals carbide/nitrides (MXenes), $\text{Ti}_3\text{C}_2\text{T}_x$ has been widely applied in energy storage, sensors, and electromagnetic shielding, owing to its outstanding electrical conductivity, tunable surface chemistry in layered structures, and high specific surface area [35–37]. For example, Xu et al. demonstrated a $\text{Ti}_3\text{C}_2\text{T}_x$ based MSC using the hybrid architecture electrode of $\text{Ti}_3\text{C}_2\text{T}_x$ MXene/multi-walled carbon nanotubes (MWCNTs) via transfer-free filtering fabrication, which showed high areal capacitance of 6 mF cm^{-2} at a frequency of 120 Hz [38]. However, the frequency response of this kind of MSCs was limited with the f_0 around 1 kHz due to compact film-type electrode where the charge transport in thick layered structure cannot instantly respond to surface ions-electrons transfer process. Further, Jiang et al. demonstrated the MXene MSCs with high volumetric capacitance (30F cm^{-3} at 120 Hz) and kilo Hertz (kHz) feature. Moreover, it retained a capacitive behavior even at high

scan rate of 300 V s^{-1} , displaying high-rate capability [39]. Unfortunately, the reported MXene based MSCs showed the limited cell voltage of 0.6 V associated with the polarization in aqueous electrolyte [40]. Therefore, it is urgently required to explore high-voltage $\text{Ti}_3\text{C}_2\text{T}_x$ MXene based MSCs applied as FCs with high frequency response.

Herein, the on-chip ultrahigh-rate MSCs based on small-sized $\text{Ti}_3\text{C}_2\text{T}_x$ MXene (M-MSCs) are fabricated in wafer-scale for AC line-filtering by photolithography microfabrication technique. The effect of thickness and interspace of microelectrodes on the frequency characteristic is primarily explored to realize the optimized device architecture. Subsequently, the resulting M-MSCs showed an areal capacitance of 153 $\mu\text{F cm}^{-2}$, a frequency characteristic over kHz range and high scan rate of 2000 V s^{-1} in aqueous electrolyte. Further, high-voltage (2 V) M-MSCs in ionic liquid electrolyte can catch up to a maximum scan rate of 5000 V s^{-1} owing to the fast ions surface accommodation. Notably, the M-MSCs pack connected in series or parallel is evidenced, showing excellent performance uniformity. Finally, the M-MSCs array is demonstrated in an AC line-filtering circuit for electrical AC conversion of versatile waveforms and frequencies.

2. Experimental

2.1. Preparation of $\text{Ti}_3\text{C}_2\text{T}_x$ MXene

The $\text{Ti}_3\text{C}_2\text{T}_x$ nanosheets were prepared through the LiF/HCl etching from Ti_3AlC_2 MAX [41]. Then, the synthesized 5 mg mL^{-1}

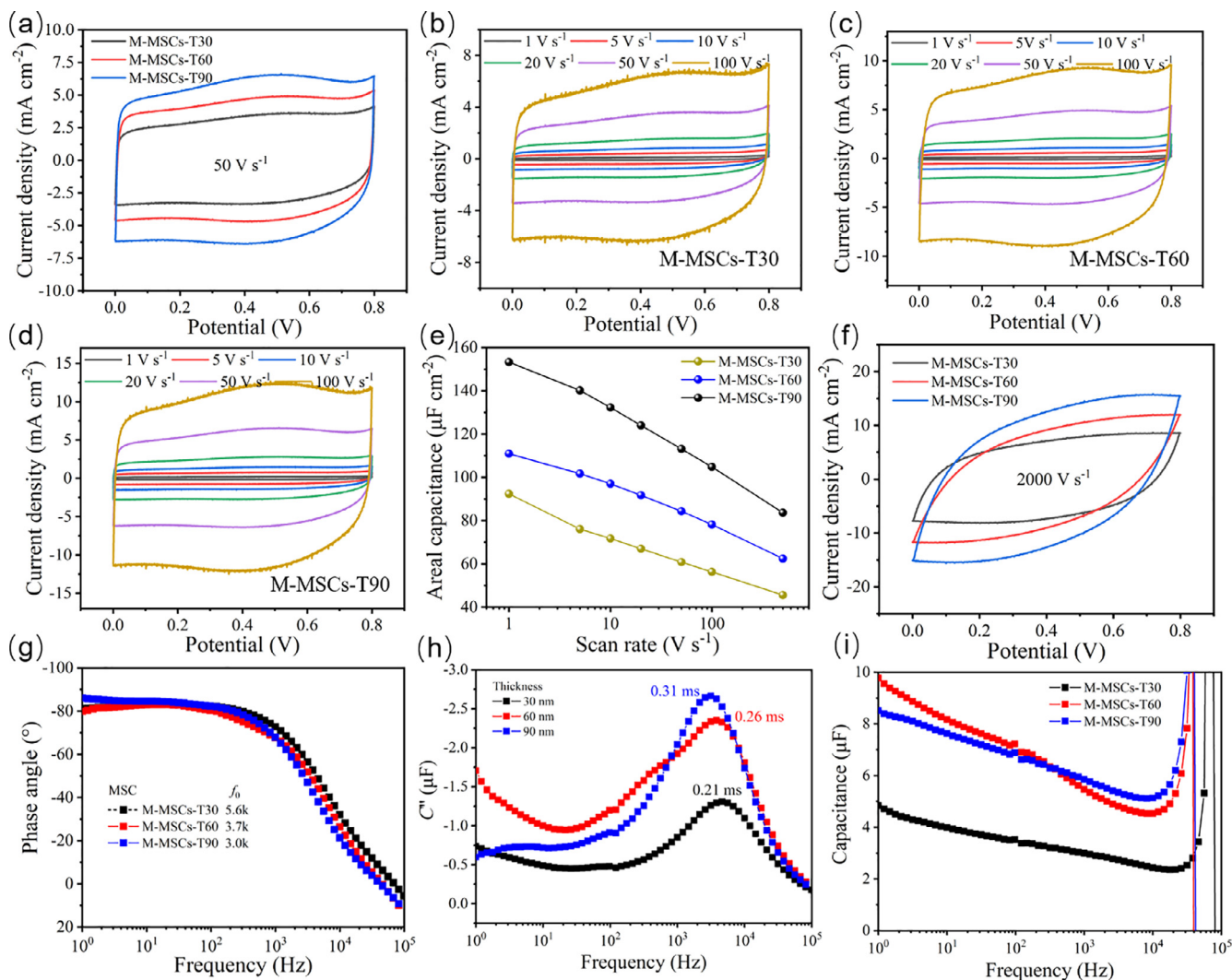


Fig. 2. Electrochemical performance of M-MSCs-T30, M-MSCs-T60 and M-MSCs-T90 tested in 1 M H_2SO_4 . (a) CV curves of M-MSCs-T30, M-MSCs-T60 and M-MSCs-T90 at a scan rate of 50 V s^{-1} . (b–d) CV curves at different scan rates of (b) M-MSCs-T30, (c) M-MSCs-T60 and (d) M-MSCs-T90. (e) Specific areal capacitance of M-MSCs-T30, M-MSCs-T60 and M-MSCs-T90 at different scan rates. (f) CV curves of M-MSCs-T30, M-MSCs-T60 and M-MSCs-T90 at 2000 V s^{-1} . (g) Bode plots, (h) plot of C' versus frequency, and (i) plot of specific capacitance versus frequency of M-MSCs-T30, M-MSCs-T60 and M-MSCs-T90.

$\text{Ti}_3\text{C}_2\text{T}_x$ solution was ultrasonicated for 2 h and centrifuged to obtain a suspension with small-sized $\text{Ti}_3\text{C}_2\text{T}_x$ nanosheets. In the preparation progress, MXene suspension was stored in the sealed bottle during ultrasonication to avoid oxidation. To prevent the increase of water temperature during ultrasonication, several ice bags were placed around the sealed bottle.

2.2. Fabrication of MSCs

The fabrication process of M-MSCs through photolithography technique is schematically illustrated in Fig. 1(a). Firstly, a 4-inch silicon wafer covered by a 300 nm SiO_2 surface layer was prepared as the substrate and then ultrasonicated in acetone and alcohol. Then, an interdigitated photoresist pattern was defined on this wafer by spin-coating, UV exposure and development. Next, a Ti/Au metal layer was thermally evaporated onto the patterned photoresist as current collector by electron beam equipment. It is noted that the Ti buffer layer was constructed to prevent the Au layer dropping from the silicon wafer. Then, the Au layer was treated with O_2 plasma to make microelectrode materials adhere well on the metal layer. Subsequently, the prepared $\text{Ti}_3\text{C}_2\text{T}_x$ MXene nanosheets were spray-coated on the metal surface to form micro-

electrode films (Fig. 1c and d) at 70°C . Finally, the whole 4-inch wafer was soaked in acetone by ultrasonication to remove the photoresist. As shown by in the inset of Fig. 1(d), the M-MSCs were efficiently fabricated compatible with large-scale manufacture and easy integration with silicon-based electronics.

2.3. Measurement and characterization

The morphological characterization of the electrode materials was performed using scanning electron microscope (SEM, Quanta 200F, FEI, USA) and a Bruker multimode 8 atomic force microscope (AFM Bruker Dimension ICON). The structural characterization of the electrode materials was performed using high-resolution X-ray diffraction (XRD, D8 Discovery, Bruker, Germany), and Raman spectroscopy system (Lab Ram HR 800, Horiba JY, Japan). The M-MSCs were tested in the electrolyte of 1 M H_2SO_4 and EMIMBF₄, respectively. Electrochemical test was carried on a CHI760E electrochemical workstation (CH Instruments China). The cyclic voltammetry (CV), galvanostatic charge/discharge (GCD) and electrochemical impedance spectra (EIS) were tested in two-electrode system. Specifically, EIS was performed in the frequency range from 0.01 Hz to 100 kHz at an open-circuit voltage with an ampli-

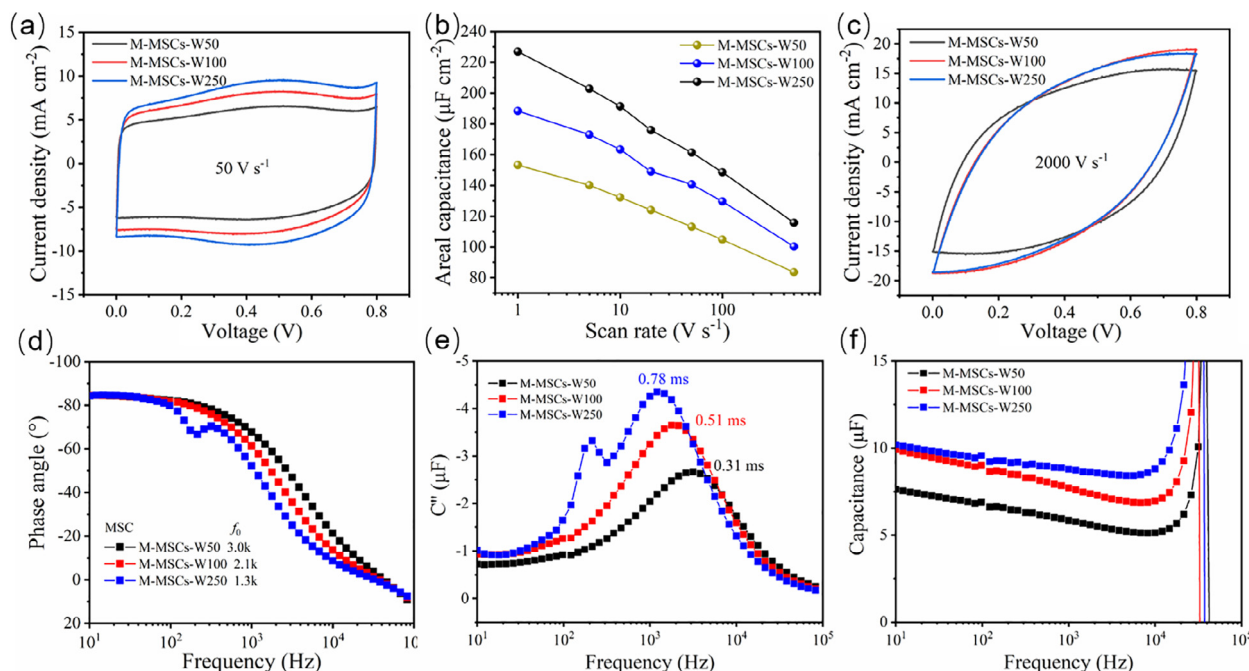


Fig. 3. Electrochemical performance of M-MSCs-W50, M-MSCs-W100 and M-MSCs-W250 tested in 1 M H₂SO₄. (a) The CV curves of M-MSCs-W50, M-MSCs-W100 and M-MSCs-W250 at the scan rate of 50 V s⁻¹, (b) Areal capacitance at different scan rates, (c) CV curves at 2000 V s⁻¹, (d) Bode plots, (e) plot of C'' versus frequency, and (f) plot of specific capacitance versus frequency of M-MSCs-W50, M-MSCs-W100 and M-MSCs-W250.

tude of 5 mV. The waveform in AC line-filtering circuits was produced in an AFG1000 signal generator (Tektronix, America) and the output was displayed in a MDO34 mixed domain oscilloscope (Tektronix, America).

3. Results and discussion

3.1. Ti₃C₂T_x MXene microelectrodes

The morphology of Ti₃C₂T_x MXene nanosheets and microelectrodes were characterized as shown in Fig. 1b–f. The appearance of (002) characteristic peaks of Ti₃C₂T_x at 6.6° (Fig. 1g) observed by XRD pattern confirmed the crystal structure [28]. Further, Raman spectroscopy was used to characterize the chemical and termination species of the Ti₃C₂T_x nanosheets (Fig. 1h). The peak at around 154, 207, 416 and 622 cm⁻¹ matched well with the literature [42], indicative of Ti₃C₂T_x MXene. As shown in Fig. 1(b), Ti₃C₂T_x MXene nanosheets displayed a lateral size of 0.8 ~ 1 μm (Fig. S1) and single-layer thickness of 1.49 nm obtained from atomic force microscope (AFM) image (Fig. 1e and f). The Ti₃C₂T_x solution was treated by sonication to decrease the size of nanosheets considering the following aspects. First, small-sized Ti₃C₂T_x nanosheets have abundant surface defects in the form of edge defects which could provide ample sites for ionic adsorption to improve electrochemical performance [43]. Second, the small-sized Ti₃C₂T_x nanosheets lie loosely with each other on the surface of microelectrodes, so the gaps between these nanosheets are beneficial for electrolyte permeation. Further, the formed film could facilitate the access of acetone resulting in easy photoresist removal in the last step of peel-off process.

3.2. Electrochemical performance

The electrochemical performances of the resulting M-MSCs based on high electrical conductive MXene films (~2200 S cm⁻¹, [15]) were shown in Fig. 2 to evaluate the frequency characteris-

tics. In addition, it is well known that the thickness of microelectrode is a critical parameter in determining the frequency characteristic since it affects the ionic accessibility and diffusion length. Especially for MSCs, decreasing the thickness to nanometer level can heavily enhance f_0 by orders of magnitude [44]. As a consequence, the electrochemical performances of M-MSCs with different microelectrode thicknesses of 30, 60 and 90 nm (Fig. S2), denoted as M-MSCs-T30, M-MSCs-T60 and M-MSCs-T90, were explored in 1 M H₂SO₄ electrolyte (Fig. 2). The width and gap between the adjacent interdigital microelectrodes are both 50 μm, and the total active area is 0.09 cm² (Fig. S3). The metal layer could avoid the accumulation of charge and excessive polarization of Ti₃C₂T_x MXene at high potential states [28], thus the M-MSCs had a voltage of 0.8 V (Fig. 2a). As expected, the thickest device M-MSCs-T90 showed a larger charge/discharge current density and integrated area in cyclic voltammetry (CV) curve compared with M-MSCs-T30 and M-MSCs-T60 (Fig. 2a), because the loading of active material was larger. The CV curves of M-MSCs with different thickness were depicted in Fig. 2(b–d) with the scan rates ranging from 1 to 100 V s⁻¹. All CV curves showed a similar rectangular shape corresponding to the pseudocapacitive behavior of reversible surface redox reaction with the valence change of Ti [45]. The relevant areal capacitance of M-MSCs (Fig. S4) was presented in Fig. 2(e), showing areal capacitance of 153 μF cm⁻² at 1 V s⁻¹. Further, M-MSCs could achieve a high scan rate of 2000 V s⁻¹ (Fig. 2g), indicative of high-power characteristic. The results of frequency characteristic were shown in Fig. 2(g–h), all cells had a large f_0 over kHz, the highest f_0 is 5.6 kHz in M-MSCs-T30, and a stable phase angle around -80° in Fig. 2(g). It is indicated that the fabricated M-MSCs could effectively act as FCs. Specifically, these relaxation time constants (τ_0) could be achieved and the corresponding f_0 can reach up to 5.6 kHz for M-MSCs-T30 (Fig. 2h). The specific capacitance decreased gradually with increasing frequency (Fig. 2i) because the migration rate of ions in electrolyte could not catch up with the rate of frequency oscillation. Although the capacitance in a single cell was slightly lower than AECs (47 μF, $f_0 < 1$ kHz), the integrated MSCs array could be

easily fabricated to satisfy the demand in capacitance and frequency.

Besides the thickness, the different widths of microelectrodes were also employed to access their influence on frequency response, realized by fabricating M-MSCs with the same gaps (50 μm) and thickness (90 nm) but different electrode widths of 50, 100 and 250 μm . The corresponding microdevices were denoted as M-MSCs-W50, M-MSCs-W100, and M-MSCs-W250 (Fig. S5). Fig. 3(a) showed similar rectangular CV lines at 50 V s^{-1} , and M-MSCs-W250 displayed the largest integrated area due to the highest loading of active materials. The specific capacitance as shown in Fig. 3(b) was also increased following the enlargement of width. The highest areal capacitance was 227 $\mu\text{F cm}^{-2}$ at 1 V s^{-1} for M-MSCs-W250. When the scan rate was up to 2000 V s^{-1} , the CV curves of M-MSCs-W250 seemed anamorphic compared with M-MSCs-W50, indicating that increasing widths would lead to a decrement in rate performance. Similarly, the f_0 in Fig. 3(d) decreased to 1.3 k for M-MSCs-W250, corresponding to a large τ_0 of 0.78 ms. It was proposed that M-MSCs-W50 had more nanosheets with exposed edges compared to others in the same cell area, which produced stronger electric force on charge and played a great role in frequency response [46]. In addition, the phase angle in these devices remained around -80° in low frequency, showing a typical capacitive feature as FCs. Moreover,

from Fig. 3(f) it is clear that the capacitance was improved at a larger width, manifesting that a desired value of capacitance or f_0 in MSCs for FCs application could be realized by controlling the width and thickness. Furthermore, the stability of M-MSCs-W250 was investigated (Fig. S6a), which showed a capacitance retention of 84.6% after 4000 cycles, demonstrative of excellent long-term stability. The slight capacitance attenuation was caused by the incomplete reversible reaction and oxidation of $\text{Ti}_3\text{C}_2\text{T}_x$ under high anodic potentials [47].

To improve the voltage range of a single cell, the ionic liquid of 1-ethyl-3-methylimidazolium tetrafluoroborate (EMIMBF₄) was selected as electrolyte due to the high ionic conductivity of 13.6 mS cm^{-1} and high stable potential windows (>4.0 V) [48]. The M-MSCs showed an available voltage of 2 V (Fig. S7) [49], and a quasi-rectangular shaped CV curve (Fig. 4a and b) in EMIMBF₄ electrolyte, denoted as M-MSCs-IL-100 and M-MSCs-IL-250. Compared with the aqueous electrolyte, M-MSCs-IL displayed a smaller capacitance in Fig. 4(c and f), because the high viscosity and large ionic size limit the electrolyte immersion and ions intercalation into $\text{Ti}_3\text{C}_2\text{T}_x$ layer in vertical direction [50]. Notably, M-MSCs-IL could reach an ultrahigh scan rate of up to 5000 V s^{-1} with electric double-layer capacitive behavior, indicating that M-MSCs-IL can simultaneously satisfy the requirement of large voltage and high power. Moreover, the f_0 in Fig. 4(e) was 6.6 kHz for M-MSCs-IL-

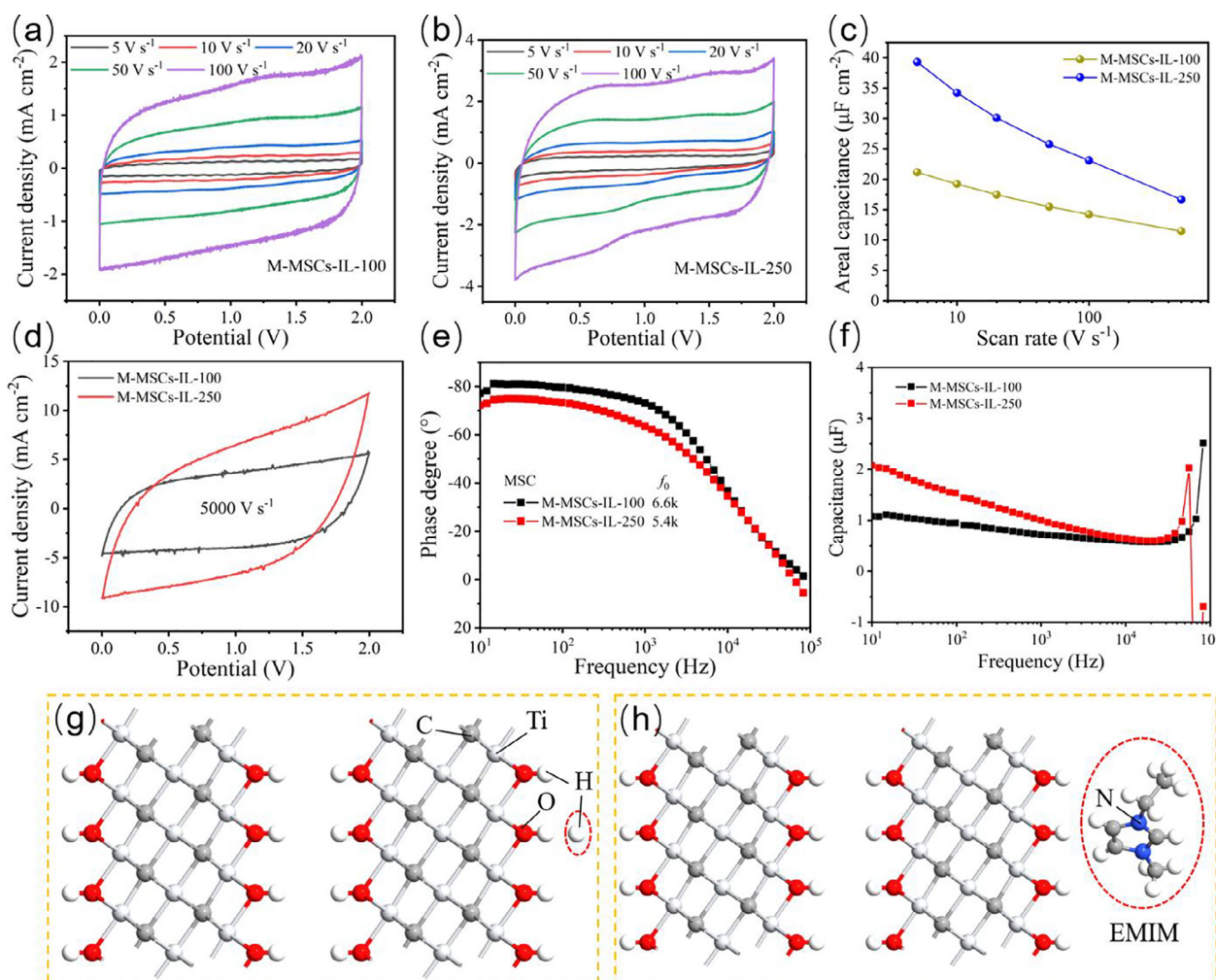


Fig. 4. Electrochemical performance of M-MSCs-IL-100 and M-MSCs-IL-250 tested in EMIMBF₄. (a and b) The CV curves of (a) M-MSCs-IL-100 and (b) M-MSCs-IL-250. (c) Areal capacitance of M-MSCs-IL-100 and M-MSCs-IL-250 at different scan rates. (d) CV curves of at 5000 V s^{-1} , (e) Bode plots, and (f) plot of specific capacitance versus frequency of M-MSCs-IL-100 and M-MSCs-IL-250. Side views of the adsorption model of different cations in electrolytes and $\text{Ti}_3\text{C}_2\text{T}_x$. (g-h) The adsorption energy calculation of cations (g) H^+ in H_2SO_4 electrolyte, and (h) EMIM⁺ in EMIMBF₄ electrolyte with $\text{Ti}_3\text{C}_2\text{T}_x$.

100, indicating that the ionic liquid was also suitable for FCs even though the ionic conductivity of EMIMBF₄ electrolyte was less than the aqueous electrolyte ($>100 \text{ mS cm}^{-1}$) [51]. In addition, M-MSCs-IL-250 displayed very excellent stability with a remarkable capacitance even after 10000 cycles (Fig. S6b).

In order to explore the influence of different electrolytes on the frequency characteristic in these M-MSCs, the adsorption energy of cations (H^+ or EMIM^+) in electrolytes and $\text{Ti}_3\text{C}_2\text{T}_x$ was calculated using density functional theory (DFT) simulation, where the model of surface terminal was built with hydroxyl group ($-\text{OH}$) considering that $-\text{OH}$ was dominating in surface functional groups. The completed structural models with two kinds of cations were depicted in Fig. 4(g–h). It is clearly revealed that terminal atoms occupied on the top sites of the centro-Ti atoms, which was in good agreement with previous studies [32]. Particularly, the adsorption energy between EMIM^+ and $\text{Ti}_3\text{C}_2\text{T}_x$ showed a lower value of -0.74 eV in Table S1 while that was -3.08 eV in the H^+ -contained model, indicating that the EMIM^+ was more easily adsorbed on the surface of $\text{Ti}_3\text{C}_2\text{T}_x$. Therefore, the lower adsorption energy would contribute to the fast adsorption/desorption of cations in electrolytes, resulting in the remarkably higher frequency characteristic of M-MSCs in ionic liquid.

To highlight the advancement of our high-frequency M-MSCs, we summarized the comparative frequency performance of M-MSCs and previously reported MSCs in Table S2. It can be seen that the frequency characteristic in this work is impressive with the large f_0 (maximum value of 5.6 kHz in $1 \text{ M H}_2\text{SO}_4$ and 6.6 kHz in EMIMBF_4) and phase angle (Φ_{120} is around -82° in $1 \text{ M H}_2\text{SO}_4$ and -79° in EMIMBF_4), which is superior to previously reported CVD graphene based MSCs with aqueous electrolyte (f_0 : 2.03 kHz ; Φ_{120} : -76.2°) and ionic liquid (f_0 : 1.15 kHz ; Φ_{120} : -60°) [22], and single-walled carbon nanotube (SWCNT) based MSCs (f_0 : 1.27 kHz ; Φ_{120} : -73°) [52]. This excellent result in frequency response indicated that M-MSCs will be applicable as FCs in the kHz AC line-filtering. Furthermore, the Ragone plot was displayed in Fig. S8 by comparing our M-MSCs with other reported MSCs for AC line-filtering. It was observed that M-MSCs exhibited

the maximum energy density of 2.2 mWh cm^{-3} at a power density of 10.8 mW cm^{-3} in aqueous electrolyte, and energy density of 3.36 mWh cm^{-3} at power density of 30.2 mW cm^{-3} in ionic liquid, which is well comparable with those of other MSCs, such as poly(3,4-ethylenedioxythiophene) (PEDOT) MSCs (7.7 mWh cm^{-3}) [53], CVD graphene MSCs (23 mWh cm^{-3}) [22], PbPPy MSCs (4.6 mWh cm^{-3}) [54] and commercial $3 \text{ V}/300 \mu\text{F AEC}$ [55].

3.3. Mscs pack

To show the applicability of wafer-scale fabrication of M-MSCs, a MSCs pack was constructed and tested in aqueous electrolyte connected in series and parallel (Fig. 5). In Fig. 5(a), the CV curves of the M-MSCs in parallel displayed similar shape and increased current density with the increasing MSC units, suggesting the uniformity of each MSC unit. Further, the capacitance increased monotonically with the number of cells (Fig. 5b), while the Bode plots (Fig. 5c) displayed slight degeneration with the increasing units. To meet the requirement of high-voltage output, different number of MSC unit connected in series were constructed, illustrating a stepwise linear increase of operational voltage from 0.8 to 8 V (Fig. 5d and e). Moreover, the Bode plots for serially-connected MSCs in Fig. 5(f) showed a decreased f_0 with increasing unit number, which could be caused by the inductive impedance existing in connecting lines between each unit. Therefore, it is demonstrated that such wafer-scale MSCs arrays hold great potential for various requirements of tailored voltage and capacitance.

3.4. AC line-filtering application

To verify filtering performance of the MSCs pack in AC line-filtering circuit, the MSCs pack connected 10 cells in parallel were linked with the diode bridge (Fig. 6a and b), and the input/output signal was displayed in Fig. 6(c). It is observed that the MSCs array was employed to impart a large capacitance of $18.6 \mu\text{F}$ at 120 Hz (Fig. S9). Further, as can be seen from Fig. 6(d–k), the MSCs array

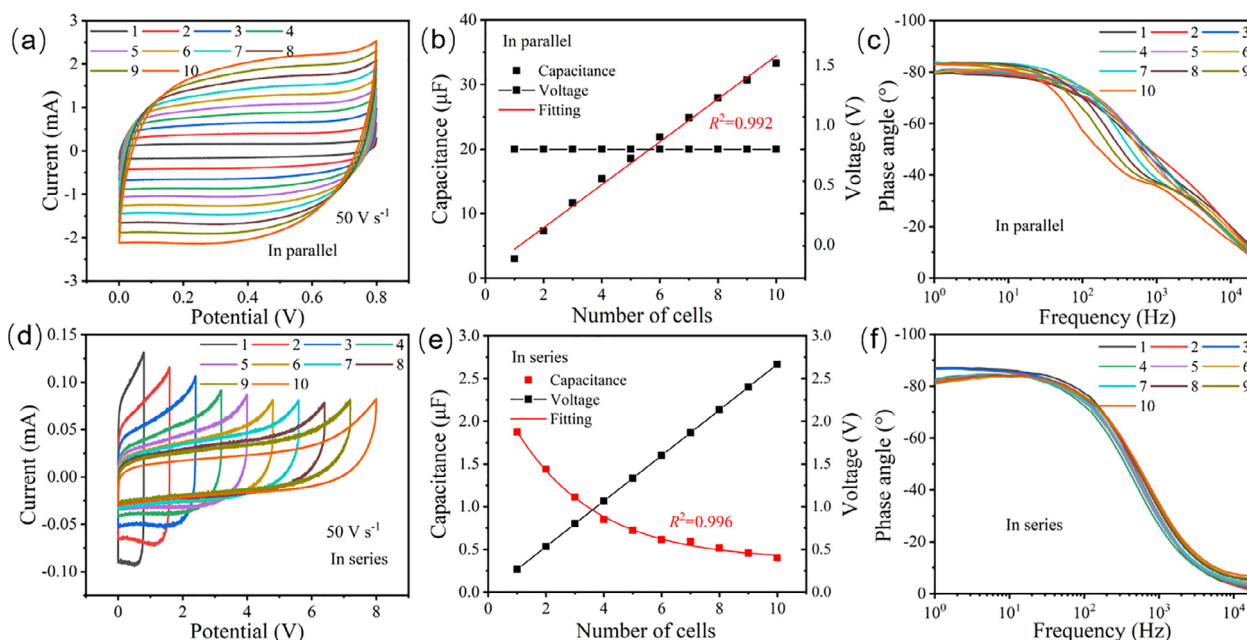


Fig. 5. Integration and performance uniformity of M-MSCs pack connected in series or in parallel in $1 \text{ M H}_2\text{SO}_4$. (a) CV curves of integrated M-MSCs connected in parallel from 1 to 10 cells, obtained at a scan rate of 50 V s^{-1} . (b) Plots of capacitance and voltage versus number of cells in parallel, R^2 is a coefficient of determination in the fitting line, and (c) phase angle versus frequency of MSCs array connected in parallel. (d) CV curves of integrated M-MSCs connected in series from 1 to 10 cells, obtained tested at a scan rate of 50 V s^{-1} . (e) plots of capacitance and voltage versus number of cells in series, and (f) phase angle versus frequency of MSCs array with 10 cells connected in series.

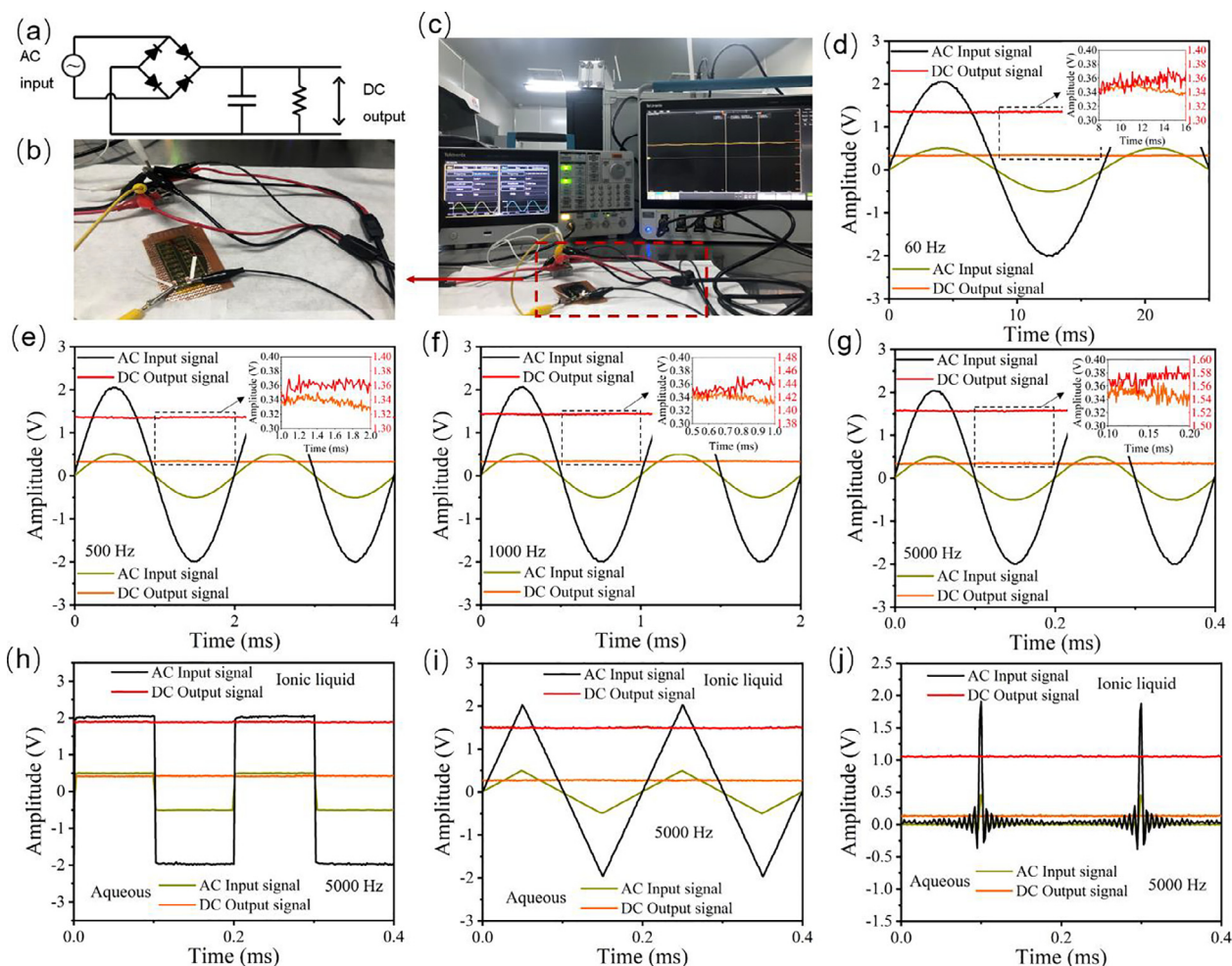


Fig 6. The performance of integrated M-MSCs pack in AC line-filtering circuit. (a) The schematic diagram of AC line-filtering circuit. (b) The photograph of actual filtering circuit composed by diode bridge and M-MSCs array. (c) The photograph showed the AC input signal in signal generator and constant DC output signal in oscilloscope. (d–g) The constant DC output signal of the AC line-filtering circuit with a sinusoidal AC input at different frequency, M-MSCs array as FCs were used in aqueous electrolyte and ionic liquid. The yellow line represented the output using aqueous electrolyte while the red line displayed the output using ionic liquid. The inset image showed the enlarge outputs in half period and the applied frequency were (d) 60 Hz, (e) 500 Hz, (f) 1000 Hz, and (g) 5000 Hz. (h–j) The constant DC output signal of the AC line-filtering circuit with various AC inputs at a frequency of 5000 Hz: (h) rectangular waveform, (i) triangle waveform, and (j) pulsed waveform.

could successfully smoothen the AC ($V_{\text{peak}} = \pm 0.5 \text{ V}$, $\pm 2 \text{ V}$) into the DC from the 60 to 5000 Hz (Fig. 6d–g) in aqueous electrolyte and ionic liquid, proving that the MSCs array had the kHz filtering capability. For comparison, an AEC (47 μF) was also applied as the FC at an AC frequency of 60 Hz and the corresponding output was shown in Fig. S10. The similar DC outputs of MSCs array (Fig. 6d) and AEC prove that the former has a filtering function comparable to commercial standards, while this MSCs array is more superior taking into consideration of integratability. In Fig. 6(d–g), the DC output signals gradually appeared the stronger ripples with increasing frequency, as presented in the enlarged images, especially in the yellow DC output lines corresponding to MSCs pack using aqueous electrolyte. This behavior showed that the filtering capability was slightly decreased, which might be caused by the decreased capacitance value in high frequency range and the enlarged capacitive resistance induced by the parallel connection. Besides the different frequency, the arbitrary AC waveform was applied with a high frequency of 5000 Hz (Fig. 6g–k). The MSCs array could efficiently rectify arbitrary AC inputs into the ideal linear outputs. The DC output voltages for sinusoidal, rectangular, triangle and pulsed waveforms were 0.33, 0.41, 0.27 and 0.14 V in aqueous electrolyte, and 1.51, 1.89, 1.49 and 1.05 V in ionic liquid, respectively. It is indicated that the DC output voltage was related to the input AC waveform.

The rectangular waveform displayed the highest DC output owing to the large average AC input voltage. In addition, the partial voltage could be drop on the diode bridge, which caused that the output voltage was less than the input peak voltage. Consequently, this MSCs array could achieve the ability to filter various input waveforms into linear ones under kHz applied frequency.

4. Conclusions

In summary, we demonstrated the wafer-scale on-chip $\text{Ti}_3\text{C}_2\text{T}_x$ MXene MSCs fabricated by photolithography technique to successfully achieve high-frequency, high-rate and miniaturized FCs. By optimizing the thickness and width of microelectrode fingers, M-MSCs exhibited excellent frequency characteristic of kHz application in aqueous electrolyte and ionic liquid. A large improvement in the voltage window (2 V) was witnessed by using ionic liquid electrolyte. Benefiting from the electrical double-layer mechanism and more low adsorption energy between cation in ionic liquid and $\text{Ti}_3\text{C}_2\text{T}_x$, M-MSCs-IL kept an impressive capacitive behavior at an ultrahigh scan rate of 5000 V s^{-1} , indicative of great applicability as high-frequency FCs with wide voltage range. Moreover, we demonstrated the facile fabrication of integrated MSCs connected in series and parallel with uniform performance to realize tailored

capacitance in various frequency ranges. Furthermore, the MSCs pack was utilized as the FC in AC line-filtering circuits, realizing various high frequency AC waveforms of 5000 Hz. This work will open new opportunities to produce wafer-scale fabrication and on-chip integration of MSCs as FCs for AC line-filtering, and to meet different emerging demands in highly sensitive and customizable electronics.

Declaration of Competing Interest

The authors declare that they have no known competing financial interests or personal relationships that could have appeared to influence the work reported in this paper.

Acknowledgments

This work was financially supported by the Natural Science Basic Research Plan in Shaanxi Province of China (2019ZDLGY16-02), the Youth Science and Technology Nova Program of Shaanxi Province (2020KJXX-068), the Fundamental Research Funds for the Central Universities (JBF201101), the National Key R&D Program of China (2016YFA0200200), the National Natural Science Foundation of China (22125903, 51872283, 22075279, 21805273, 22109160), the Liao Ning Revitalization Talents Program (XLYC1807153), the Liaoning BaiQianWan Talents Program, Dalian Innovation Support Plan for High Level Talents (2019RT09), the Dalian National Laboratory For Clean Energy (DNL), CAS, DNL Cooperation Fund, CAS (DNL201912, DNL201915, DNL202016, DNL202019), DICP (DICP ZZBS201708, DICP ZZBS201802, DICP I2020032), the Joint Fund of the Yulin University and the Dalian National Laboratory for Clean Energy (YLU-DNL Fund 2021002, 2021009), and the China Postdoctoral Science Foundation (2021M693126, 2021M693127, 2019M661141, 2020M680995).

Appendix A. Supplementary data

Supplementary data to this article can be found online at <https://doi.org/10.1016/j.jechem.2021.11.012>.

References

- [1] S. Xu, Y. Qin, C. Xu, Y. Wei, R. Yang, Z.L. Wang, *Nat. Nanotechnol.* 5 (2010) 366–373.
- [2] L. Yin, K.N. Kim, J. Lv, F. Tehrani, M. Lin, Z. Lin, J.-M. Moon, J. Ma, J. Yu, S. Xu, J. Wang, *Nat. Commun.* 12 (2021) 1542.
- [3] J. Park, J. Kim, S.-Y. Kim, W.H. Cheong, J. Jang, Y.-G. Park, K. Na, Y.-T. Kim, J.H. Heo, C.Y. Lee, J.H. Lee, F. Bien, J.-U. Park, *Sci. Adv.* 4 (2018) eaap9841.
- [4] R. Kumar, J. Shin, L. Yin, J.-M. You, Y.S. Meng, J. Wang, *Adv. Energy Mater.* 7 (2017) 1602096.
- [5] J. Qin, J. Gao, X. Shi, J. Chang, Y. Dong, S. Zheng, X. Wang, L. Feng, Z.S. Wu, *Adv. Funct. Mater.* 30 (2020) 1909756.
- [6] S. Zheng, H. Wang, P. Das, Y. Zhang, Y. Cao, J. Ma, S.F. Liu, Z.S. Wu, *Adv. Mater.* 33 (2021) e2005449.
- [7] X. Cheng, W. Tang, Y. Song, H. Chen, H. Zhang, Z.L. Wang, *Nano Energy* 61 (2019) 517–532.
- [8] B. He, P. Man, Q. Zhang, H. Fu, Z. Zhou, C. Li, Q. Li, L. Wei, Y. Yao, *Nano-Micro Lett.* 11 (2019) 101.
- [9] C. Li, Q. Zhang, J. Sun, T. Li, S. E. Z. Zhu, B. He, Z. Zhou, Q. Li, Y. Yao, *ACS Energy Lett.* 3 (2018) 2761–2768.
- [10] F. Xi, Y. Pang, W. Li, T. Jiang, L. Zhang, T. Guo, G. Liu, C. Zhang, Z.L. Wang, *Nano Energy* 37 (2017) 168–176.
- [11] C. Wu, A.C. Wang, W. Ding, H. Guo, Z.L. Wang, *Adv. Energy Mater.* 9 (2019) 1802906.
- [12] N. Islam, S. Li, G. Ren, Y. Zu, J. Warzywoda, S. Wang, Z. Fan, *Nano Energy* 40 (2017) 107–114.
- [13] Y. Wang, Y. Zhao, L. Qu, *J. Energy Chem.* 59 (2021) 642–665.
- [14] S. Zheng, X. Shi, P. Das, Z.S. Wu, X. Bao, *Adv. Mater.* 31 (2019) e1900583.
- [15] S. Zheng, C. Zhang, F. Zhou, Y. Dong, X. Shi, V. Nicolosi, Z.-S. Wu, X. Bao, *J. Mater. Chem. A* 7 (2019) 9478–9485.
- [16] F. Zhou, H. Huang, C. Xiao, S. Zheng, X. Shi, J. Qin, Q. Fu, X. Bao, X. Feng, K. Müllen, Z.S. Wu, *J. Am. Chem. Soc.* 140 (2018) 8198–8205.
- [17] X. Shi, L. Tian, S. Wang, P. Wen, M. Su, H. Xiao, P. Das, F. Zhou, Z. Liu, C. Sun, Z.-S. Wu, X. Bao, *J. Energy Chem.* 52 (2021) 284–290.
- [18] Q. Zhang, W. Xu, J. Sun, Z. Pan, J. Zhao, X. Wang, J. Zhang, P. Man, J. Guo, Z. Zhou, B. He, Z. Zhang, Q. Li, Y. Zhang, L. Xu, Y. Yao, *Nano Lett.* 17 (2017) 7552–7560.
- [19] Z. Zhou, Q. Zhang, J. Sun, B. He, J. Guo, Q. Li, C. Li, L. Xie, Y. Yao, *ACS Nano* 12 (2018) 9333–9341.
- [20] K.U. Laszczyk, K. Kobashi, S. Sakurai, A. Sekiguchi, D.N. Futaba, T. Yamada, K. Hata, *Adv. Energy Mater.* 5 (2015) 1500741.
- [21] Z.-S. Wu, Z. Liu, K. Parvez, X. Feng, K. Müllen, *Adv. Mater.* 27 (2015) 3669–3675.
- [22] J. Ye, H. Tan, S. Wu, K. Ni, F. Pan, J. Liu, Z. Tao, Y. Qu, H. Ji, P. Simon, Y. Zhu, *Adv. Mater.* 30 (2018) e1801384.
- [23] P. Huang, C. Lethien, S. Pinaud, K. Brousse, R. Laloo, V. Turq, M. Respaud, A. Demortière, B. Daffos, P.L. Taberna, B. Chaudret, Y. Gogotsi, P. Simon, *Science* 351 (2016) 691.
- [24] J. Han, Y.C. Lin, L. Chen, Y.C. Tsai, Y. Ito, X. Guo, A. Hirata, T. Fujita, M. Esashi, T. Gessner, M. Chen, *Adv. Sci.* 2 (2015) 1500067.
- [25] C.J. Zhang, L. McKeon, M.P. Kremer, S.H. Park, O. Ronan, A. Seral-Ascaso, S. Barwich, C.O. Coileain, N. McEvoy, H.C. Nerl, B. Anasori, J.N. Coleman, Y. Gogotsi, V. Nicolosi, *Nat. Commun.* 10 (2019) 1795.
- [26] Y. Zhang, T. Ji, S. Hou, L. Zhang, Y. Shi, J. Zhao, X. Xu, *J. Power Sources* 403 (2018) 109–117.
- [27] J. Cai, C. Lv, A. Watanabe, *ACS Appl. Mater. Interfaces* 10 (2017) 915–924.
- [28] Y. Xie, H. Zhang, H. Huang, Z. Wang, Z. Xu, H. Zhao, Y. Wang, N. Chen, W. Yang, *Nano Energy* 74 (2020) 104928.
- [29] X. Mu, J. Du, Y. Li, H. Bai, H. Zhao, Z. Wei, B. Huang, Y. Sheng, Z. Zhang, E. Xie, *Carbon* 144 (2019) 228–234.
- [30] J.R. Miller, R.A. Outlaw, B.C. Holloway, *Science* 329 (2010) 1637–1639.
- [31] Q. Zhou, M. Zhang, J. Chen, J.D. Hong, G. Shi, *ACS Appl. Mater. Interfaces* 8 (2016) 20741–20747.
- [32] A. Eftekhari, *J. Mater. Chem. A* 6 (2018) 2866–2876.
- [33] M. Wu, F. Chi, H. Geng, H. Ma, M. Zhang, T. Gao, C. Li, L. Qu, *Nat. Commun.* 10 (2019) 2855.
- [34] G.S. Gund, J.H. Park, R. Harpalsinh, M. Kota, J.H. Shin, T.-I. Kim, Y. Gogotsi, H.S. Park, *Joule* 3 (2019) 164–176.
- [35] X. Zhang, Z. Zhang, Z. Zhou, *J. Energy Chem.* 27 (2018) 73–85.
- [36] X. Feng, J. Ning, B. Wang, H. Guo, M. Xia, D. Wang, J. Zhang, Z.-S. Wu, Y. Hao, *Nano Energy* 72 (2020) 104741.
- [37] C. Zhang, *J. Energy Chem.* 60 (2021) 417–434.
- [38] S. Xu, W. Liu, B. Hu, X. Wang, *Nano Energy* 58 (2019) 803–810.
- [39] Q. Jiang, N. Kurra, K. Maleski, Y. Lei, H. Liang, Y. Zhang, Y. Gogotsi, H.N. Alshareef, *Adv. Energy Mater.* 9 (2019) 1901061.
- [40] C. Zhong, Y. Deng, W. Hu, J. Qiao, L. Zhang, *J. Zhang, Chem. Soc. Rev.* 44 (2015) 7484–7539.
- [41] M. Naguib, O. Mashtalir, J. Carle, V. Presser, J. Lu, L. Hultman, Y. Gogotsi, M.W. Barsoum, *ACS Nano* 6 (2012) 1322–1331.
- [42] Q. Li, Q. Wang, L. Li, L. Yang, Y. Wang, X. Wang, H.T. Fang, *Adv. Energy Mater.* 10 (2020) 2000470.
- [43] Y.-Y. Peng, B. Akuzum, N. Kurra, M.-Q. Zhao, M. Alhabeib, B. Anasori, E.C. Kumbur, H.N. Alshareef, M.-D. Ger, Y. Gogotsi, *Energy Environ. Sci.* 9 (2016) 2847–2854.
- [44] Z. Zhang, M. Liu, X. Tian, P. Xu, C. Fu, S. Wang, Y. Liu, *Nano Energy* 50 (2018) 182–191.
- [45] M. Hu, Z. Li, T. Hu, S. Zhu, C. Zhang, X. Wang, *ACS Nano* 10 (2016) 11344–11350.
- [46] M.K. Hota, Q. Jiang, Y. Mashraei, K.N. Salama, H.N. Alshareef, *Adv. Electron. Mater.* 3 (2017) 1700185.
- [47] Y. Dall'Agnese, P. Rozier, P.-L. Taberna, Y. Gogotsi, P. Simon, *J. Power Sources* 306 (2016) 510–515.
- [48] R. Hagiwara, J.S. Lee, *Electrochemistry* 75 (2007) 23–34.
- [49] J. Fuller, R.T. Carlin, R.A. Osteryoung, *J. Electrochem. Soc.* 144 (1997) 3881–3886.
- [50] Z. Lin, D. Barbara, P.-L. Taberna, K.L.V. Aken, B. Anasori, Y. Gogotsi, P. Simon, *J. Power Sources* 326 (2016) 575–579.
- [51] D.C. Price, W.G. Davenport, *Metall. Trans. B* 11 (1980) 159–163.
- [52] J. Pu, X. Wang, R. Xu, S. Xu, K. Komvopoulos, *Microsyst. Nanoeng.* 4 (2018) 16.
- [53] N. Kurra, M.K. Hota, H.N. Alshareef, *Nano Energy* 13 (2015) 500–508.
- [54] K. Jiang, I.A. Baburin, P. Han, C. Yang, X. Fu, Y. Yao, J. Li, E. Cánovas, G. Seifert, J. Chen, M. Bonn, X. Feng, X. Zhuang, *Adv. Funct. Mater.* 30 (2019) 1908243.
- [55] M.F. El-Kady, V. Strong, S. Dubin, R.B. Kaner, *Science* 335 (2012) 1326.